

High- T_c Single-Component Organosilicon Ferroelectric Crystal Obtained by H/F Substitution

Hang Peng,[#] Hang Yu,[#] Shu-Yu Tang, Yu-Ling Zeng, Peng-Fei Li, Yuan-Yuan Tang, Zhi-Xu Zhang, Ren-Gen Xiong,^{*} and Han-Yue Zhang^{*}



Cite This: *JACS Au* 2023, 3, 603–609



Read Online

ACCESS |

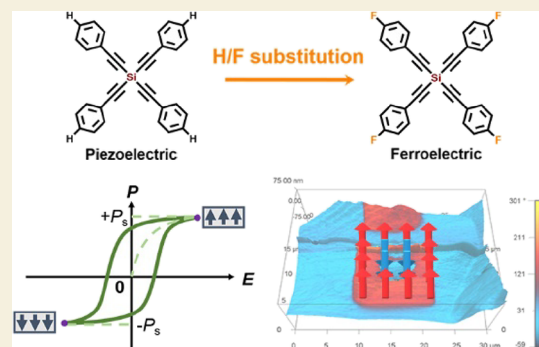
Metrics & More

Article Recommendations

Supporting Information

ABSTRACT: Organic single-component ferroelectrics are highly desirable for their low molecular mass, light weight, low processing temperature, and excellent film-forming properties. Organosilicon materials with a strong film-forming ability, weather resistance, nontoxicity, odorlessness, and physiological inertia are very suitable for device applications related to the human body. However, the discovery of high- T_c organic single-component ferroelectrics has been very scarce, and the organosilicon ones even less so. Here, we used a chemical design strategy of H/F substitution to successfully synthesize a single-component organosilicon ferroelectric tetrakis(4-fluorophenylethynyl)silane (TFPES). Systematic characterizations and theory calculations revealed that, compared with the parent nonferroelectric tetrakis(phenylethynyl)silane, fluorination caused slight modifications of the lattice environment and intermolecular interactions, inducing a $4/mmmFmm2$ -type ferroelectric phase transition at a high T_c of 475 K in TFPES. To our knowledge, this T_c should be the highest among the reported organic single-component ferroelectrics, providing a wide operating temperature range for ferroelectrics. Moreover, fluorination also brought about a significant improvement in the piezoelectric performance. Combined with excellent film properties, the discovery of TFPES provides an efficient path for designing ferroelectrics suitable for biomedical and flexible electronic devices.

KEYWORDS: organosilicone, H/F substitution, high T_c , organic single-component ferroelectrics, chemical design



Growing concerns for environmental protection and flexible and wearable devices, molecular ferroelectrics are attracting tremendous interest as a beneficial complement to inorganic ferroelectrics because of their lightweight, low processing temperature, low cost, and biocompatible characteristics.^{1–8} As the saying goes, the greatest truth is concise. Likewise, some excellent functional materials generally have a simple structure. Among molecular ferroelectrics, the organic single-component (SC) ones with a low molecular mass are desirable for application in organic electronics, by taking advantages of low acoustic impedance, mechanical flexibility, and excellent film-forming properties. Thiourea is the simplest SC ferroelectric, while its T_c is far lower than room temperature.⁹ The subsequently discovered SC ferroelectrics, 2,2,6,6-tetramethylpiperidine-*N*-oxyl and trichloroacetamide,^{10,11} also have problems of instability and a narrow ferroelectric temperature window, respectively. In 2010, notably, the report on organic SC ferroelectric croconic acid with a high spontaneous polarization indicated that organic ferroelectric crystals have the performance potential comparable to inorganic ones.¹² However, compared with the vigorous development of multicomponent ionic molecular ferroelectrics, the discovery of new organic SC ferroelectrics appears to be

stagnant. In the past decade, several excellent organic SC ferroelectrics have been discovered, including trisubstituted haloimidazoles,¹³ (*R* and *S*)-3-hydroxyquinoline,¹⁴ 2-(hydroxymethyl)-2-nitro-1,3-propanediol,¹⁵ (*R* and *S*)-10-camphorsulfonylimine,¹⁶ and spirooxazacamphorsultam derivatives.¹⁷ To date, however, small-molecule organic SC ferroelectrics remain very rare, and the high- T_c ones are even more counted on one's fingers.

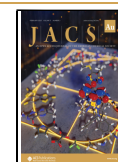
As an important key parameter, a high Curie temperature (T_c) is essential for ferroelectric-related applications as electronic components under high-temperature conditions.¹⁸ It is because of stable ferroelectricity with high T_c that the currently commercial inorganic ferroelectrics can be phenomenally applied in a variety of fields including medical, aerospace, information, and energy industries.^{19–23} Efficient methods for inducing ferroelectricity and regulating T_c have

Received: January 4, 2023

Revised: January 21, 2023

Accepted: January 26, 2023

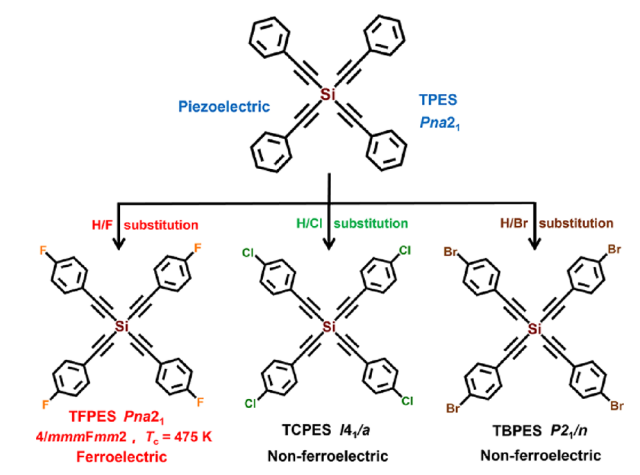
Published: February 12, 2023



been extensively studied, including strain engineering and isotope effects.^{24–26} For example, the oxygen isotope substitution enables quantum paraelectric SrTiO₃ to possess ferroelectricity,²⁷ and deuteration has been often used to enhance T_c in hydrogen-bonded ferroelectrics such as KH₂PO₄ and PbHPO₄.^{28–31} However, the applicability of these strategies is very narrow, limited to a few specific material systems. H/F substitution, resembling the H/D isotope effect, has become a more universal and effective guideline for chemically designing molecular ferroelectrics and optimizing performance.^{32–34} Because of the similar van der Waals radii and steric parameters and different electronegativity between H and F atoms, fluorination would have very little damage to the crystal structure but significantly change the physical and chemical properties. Benefiting from the phase transition mechanism of the cationic order–disorder transition, H/F substitution can significantly increase the potential energy barrier of molecular orientational motion to greatly enhance the T_c . Over the past few years, a series of high- T_c molecular ferroelectrics have been successfully designed using the H/F substitution strategy, including (*R*)- and (*S*)-3-*F*-(pyrrolidinium)MnCl₃,³⁵ (4-fluoroquinuclidinium)ReO₄,³⁶ (4,4-difluoropiperidinium)₂PbI₄,³⁷ and so on.^{38–42} A typical case is that H/F substitution makes the T_c increase from 190 K in the prototype (1-azabicyclo[2.2.1]heptane)CdCl₃ to 419 K in the fluorinated ferroelectric (4-fluoro-1-azabicyclo[2.2.1]heptane)CdCl₃.⁴³ It must be mentioned that, however, the effect of H/F substitution has been proven very effective for typical order–disorder-type multicomponent molecular ferroelectrics, while its role in single-component organic crystals remains unknown, especially the one with a displacive ferroelectric mechanism. Moreover, most of the reported organic ferroelectric crystals belong to certain types of organic molecules containing oxygen and nitrogen.

Notably, Zhang et al. recently reported a single-component organosilicon ferroelectric *D*-chiro-inositol-SiMe₃,⁴⁴ which shows excellent thin-film properties with superior softness, ductility, flexibility, and biocompatibility that are desirable for biomedical and human-compatible applications, offering a new structural paradigm for molecular ferroelectrics. As a class of compounds in which organic groups are connected to silicon atoms, organosilicon has the characteristics of a strong film-forming ability, hydrophobicity, corrosion resistance, high- and low-temperature resistance, weather resistance, nontoxicity, odorlessness, physiological inertia, etc.^{45–48} These attributes could bring more application possibilities for molecular ferroelectrics.^{49,50} Inspired by the H/F substitution methodology (Scheme 1), we successfully designed a single-component organosilicon ferroelectric tetrakis(4-fluorophenylethynyl)silane (TFPES). Compared with the parent tetrakis(phenylethynyl)silane (TPES) with nonferroelectricity, the fluorine substitution alters the crystal packing environment (*i.e.*, the intermolecular interactions) to trigger a *4/mmmFmm2*-type ferroelectric phase transition at a high T_c of 475 K in TFPES. In contrast, tetrakis(4-chlorophenylethynyl)silane (TCPES) and tetrakis(4-bromophenylethynyl)silane (TBPES) obtained by substitution of heavier Cl and Br atoms both have a centrosymmetric crystal structure fail to meet the polar symmetry for ferroelectrics. Density functional theory calculations revealed the similar van der Waals radii of hydrogen (1.2 Å) and fluorine (1.35 Å) and the larger electronegativity of fluorine, which results in that the packing patterns and space group (*Pna2*₁) of these two crystals do not

Scheme 1. Chemical Design Strategy of Organosilicon Ferroelectric TFPES



change significantly, and the stronger binding effect provides a higher activation energy barrier during the phase transition, thus increasing the phase transition temperature. To our knowledge, the T_c of TFPES is the highest one among the reported organic single-component ferroelectrics. Its ferroelectricity has been determined and confirmed by systematic characterizations. The thin film also shows excellently soft, pliable, and nontoxic properties of organosilicon compounds, making TFPES competitive for biomedical applications.

Single-crystal X-ray diffractions were carried out to get structural information about the stacking arrangement, the origin of polarization, and the mechanism of the phase transition. Crystal structure analysis reveals that TPES crystallizes in an orthorhombic polar *Pna2*₁ space group (Table S1), where the TPES molecules are arranged in two manners with an adjacent alternating sequence viewed from the *c*-axis direction (Figure 1a,d). Structurally, there are C–H⋯π interactions formed between one benzene ring of a TPES molecule and the C≡C bond of the adjacent TPES molecule. These weak interactions are like a rope to pull the phenylacetylene group, which make the molecular symmetry broken and tend to be slightly displaced and distorted, resulting in the generation of macroscopic polarization along the *c*-axis direction. However, unfortunately, despite great efforts, polarization switching cannot be achieved experimentally. The H/F substitution at the para position on the four benzene rings did not damage the crystal symmetry and the packing arrangement. The resulting TFPES also crystallizes in the polar *Pna2*₁ space group with the cell parameters of $a = 19.8373$ Å, $b = 6.9630$ Å, $c = 18.9233$ Å, and $V = 2613.82$ Å³ (Table S1), showing crystal polarity with spontaneous polarization along the [001] direction. Intermolecular interactions as an indispensable tool in the development of crystallographic engineering have been extensively utilized to design various functional crystals. Like the parent TPES, the polarization source of TFPES is also related to the distorted displacement and polar arrangement of molecules caused by weak intermolecular interactions (Figure 1b,e). Differently, the fluorination brings new weak F⋯π interactions between one benzene ring of the TFPES molecule and the F atom of the adjacent TFPES molecule. The C–H⋯π interactions (C⋯C distance, 3.796 Å) in the TFPES crystal are obviously weaker than those (3.726 Å) in the TPES crystal. In contrast, after H/Cl substitution, the obtained TCPES adopts a centrosym-

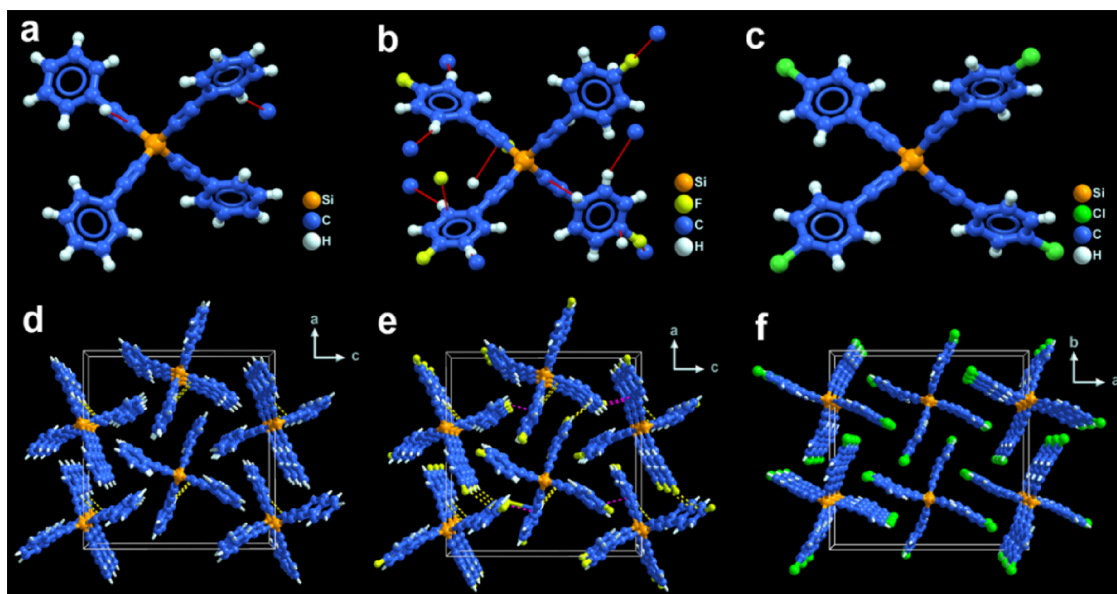


Figure 1. Crystal structures. Structural units of (a) TPES, (b) TFPES, and (c) TCPES. Packing view of unit cells of (d) TPES, (e) TFPES, and (f) TCPES. The red dotted lines represent weak interactions in Figure 1a,b. The yellow dotted lines indicate C–H $\cdots\pi$ interactions, and the pink dotted lines refers to F $\cdots\pi$ interactions.

metric crystal structure with the tetragonal $I4_1/a$ space group (Table S1). The TCPES molecules are arranged in one manner, where no apparent intermolecular interactions exist in the crystal lattice (Figure 1c,f). We further performed the related calculations of Hirshfeld d_{norm} surfaces to detect intermolecular interactions in TPES, TFPES, and TCPES. As shown in Figure S1, the clear interaction contacts (red region) can be observed in TPES and TFPES while no obvious contacts in TCPES. In general, the C–H $\cdots\pi$ interactions play a vital role in the generation of polar structures of TPES and TFPES, and the synergistic effect with weak F $\cdots\pi$ interactions in TFPES increases the greater possibility of twist displacement of molecules, providing opportunities for polarization switching.

Because of the similar van der Waals radii of hydrogen (1.2 Å) and fluorine (1.35 Å),⁵¹ the packing patterns of these two crystals do not change significantly, and both of them crystallize in the same space group ($Pna2_1$), which accords with the general law of the fluorination effect. However, when a hydrogen atom is replaced by a chlorine atom (1.8 Å) and a bromine atom (1.95 Å), the obvious difference of van der Waals radii results in a significant change in the crystallographic space group. As a consequence, TCPES and TBPES crystallize in centrosymmetric space groups $I4_1/a$ and $P2_1/n$, respectively (Figure 1c and Figure S2). We calculated the electrostatic potential of TPES, TFPES, TCPES, and TBPES molecules. As shown in Figures S3–S6, the electrostatic potentials of the atoms in position 4 of the benzene ring are 0.017, -0.015 , 0.005, and 0.012 Hartree for TPES, TFPES, TCPES, and TBPES, respectively. The large electronegativity of fluorine gives it a much lower electrostatic potential, which provides new binding sites for interactions between molecules. Such a stronger binding effect may provide a higher activation energy barrier during the order–disorder phase transition, thus increasing the phase transition temperature.

The introduction of fluorine atoms makes TFPES undergo a structural phase transition up to 475 K (T_c), which can be detected on the thermal anomaly peak by differential scanning

calorimetry measurement (Figure 2a). The temperature-dependent dielectric constant shows an anomaly around 475

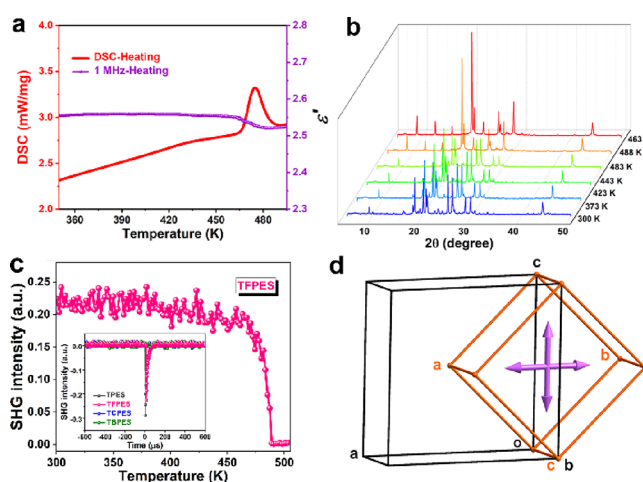


Figure 2. (a) DSC and temperature-dependent dielectric constant curves. (b) Variable-temperature PXRD patterns. (c) Temperature-dependent SHG response in the cooling process; inset: the comparison of SHG signals for TPES, TFPES, TCPES, and TBPES crystals. (d) Relationship of two cells between the ferroelectric phase (FP, black lines) and the paraelectric phase (PP, brown lines).

K as well. The existence of the phase transition demonstrates that the molecular structure pulled by weak intermolecular interactions is prone to twisting displacement, which is conducive to the reorientation of macroscopic dipole moments to cause polarization switching. It is worth noting that this T_c of 475 K is the highest one among reported organic SC ferroelectrics, much higher than other organic ferroelectrics including 2-(hydroxymethyl)-2-nitro-1,3-propanediol (345 K),¹⁵ (R and S)-3-quinuclidinol (400 K),¹⁴ (R and S)-10-camphorsulfonylimine (429 K),¹⁶ (R)-BINOL–DIPASi (362 K), and (S)-BINOL–DIPASi (363 K)⁵⁰ and greater than that of the inorganic ferroelectric BaTiO₃ (393 K).¹⁹ In addition,

chemical group modification also brings about an increase in the crystal melting point, and the melting points of TPES, TFPES, TCPES, and TBPEs were determined at 480, 511, 577, and 565 K, respectively (Figure S7). This indicates that the TFPES crystal has a stable paraelectric phase. We attempted to determine the crystal structure in the paraelectric phase, but unfortunately, the X-ray diffraction of the crystal at high temperatures was too weak to succeed in obtaining an accurate structure. Powder X-ray diffraction (PXRD) can also provide some valuable information about crystal symmetry, and thus, we further carried out variable-temperature PXRD measurements. As illustrated in Figure 2b, the PXRD patterns remain almost unchanged in the temperature range of 300–463 K, while the patterns above 475 K experience obvious changes in both the number and positions of diffraction peaks, indicating the occurrence of the phase transition with symmetry changes. Indexing and refinement of PXRD data at 573 K reveal a tetragonal point group $4/mmm$ with the cell parameters of $a = 19.8838 \text{ \AA}$, $b = 19.8838 \text{ \AA}$, $c = 7.1041 \text{ \AA}$, and $V = 2808.73 \text{ \AA}^3$ (Figure S8a). The direction of two cells between the ferroelectric phase (FP) and the paraelectric phase (PP) follows the relationship: $a_{FP} (19.8373 \text{ \AA}) \leftrightarrow a_{PP} (19.8838 \text{ \AA}) - b_{PP} (19.8838 \text{ \AA})$, $b_{FP} (6.96300 \text{ \AA}) \leftrightarrow c_{PP} (7.1041 \text{ \AA})$, $c_{FP} (7.1041 \text{ \AA}) \leftrightarrow a_{PP} (19.8838 \text{ \AA}) + b_{PP} (19.8838 \text{ \AA})$ (Figure 2d). In this case, the $[001]$ direction in FP corresponds to the $[110]$ direction in PP, which meets the symmetry requirements of the $4/mmmFmm2(s)$ -type ferroelectric phase transition defined by the Aizu rule.⁵² The second harmonic generation (SHG) response of the synthesized crystals at room temperature verifies the polar $Pna2_1$ space group of TPES and TFPES (inset of Figure 2c). Furthermore, with the increase in temperature, the SHG response remains unchanged and then abruptly drops to zero in the vicinity of T_c , which is in good agreement with the occurrence of a $4/mmmFmm2(s)$ -type ferroelectric phase transition (Figure 2c).

To determine the ferroelectricity of TFPES, we used the double-wave method to measure the relationship between polarization (P) and voltage (V). As shown in Figure 3, two current peaks in opposite directions represent two equivalent polarization states. The obtained P – V curve presents a typical well-shaped hysteresis loop, proving its ferroelectricity. The orientation of the measured thin film was verified by comparison between the measured powder X-ray diffraction

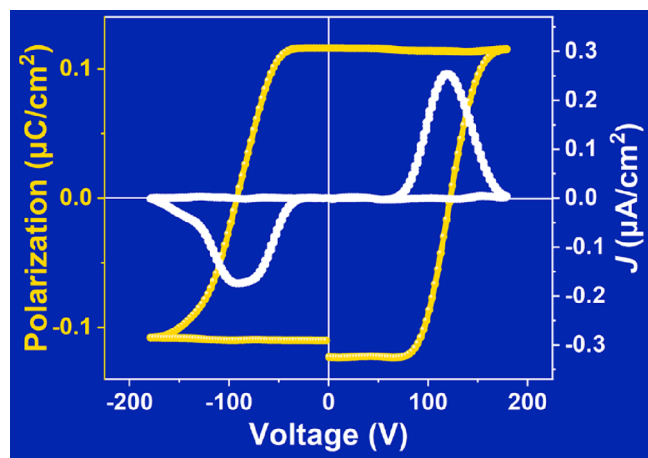


Figure 3. Polarization–voltage hysteresis loop of TFPES measured on its thin film.

pattern on the thin film of TFPES and the one simulated by its crystal data at 300 K (Figure S8b). We further studied the ferroelectric behaviors of TFPES in its thin films through piezoresponse force microscopy (PFM) measurements. Although most regions of the thin film are in a single-domain state, domain structures are still observed in some regions. Typical as-grown ferroelectric domains are revealed by vertical PFM mappings, as shown in Figure 4a–c, which exhibit an

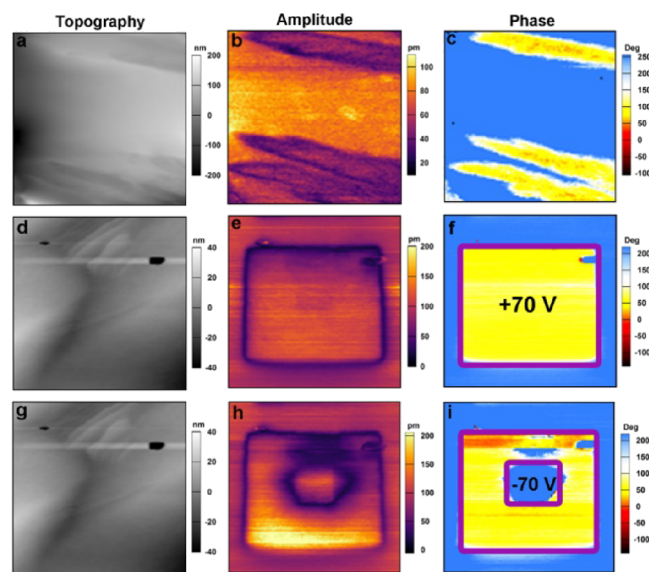


Figure 4. PFM measurements for the thin film of TFPES. (a–c) Domain structure observed in the TFPES thin film: (a) topography, (b) vertical PFM amplitude, and corresponding (c) PFM phase images. (d–i) Vertical PFM images of the TFPES thin film indicating ferroelectric polarization switching. Topography (left), amplitude (middle), and phase (right) images for the $15 \times 15 \mu\text{m}^2$ area, which were taken (d–f) after applying tip biases of +70 V and (g–i) subsequently -70 V in the central region.

irregular shape and have no crosstalk with the surface morphology. Then, we performed local domain switching experiments to directly visualize the polarization switching, where the above-mentioned single-domain pattern was used as an initial state. When a DC tip voltage of +70 V was used to scan the central region marked by a purple box, the subsequent PFM imaging revealed a new domain, indicating that the polarization can be reoriented by the external electric field (Figure 4d–f). Moreover, the polarization in the new domain can be switched back by applying an opposite tip voltage of -70 V (Figure 4g–i). Meanwhile, the surface morphology of the scanned region remains constant during the above electrical writing. PFM hysteresis loops shown in Figure 5a,b further demonstrate the ferroelectric nature of TFPES, wherein the local coercive voltage is about 47 V. All the above PFM pieces of evidence unambiguously establish the existence of ferroelectricity in the TFPES crystal.

An AC bias across the resonant frequency was applied to the PFM tip to drive the crystals of TPES and TFPES along the c -axis under vertical PFM mode, and the vibration was recorded at the same frequency. Information on the vibration, such as the amplitude, phase, resonant frequency, and quality factor, can be fitted by the simple harmonic oscillator (SHO) model.⁵³ The amplitude was enhanced and amplified by the Q factor. Therefore, the intrinsic amplitude can be obtained by

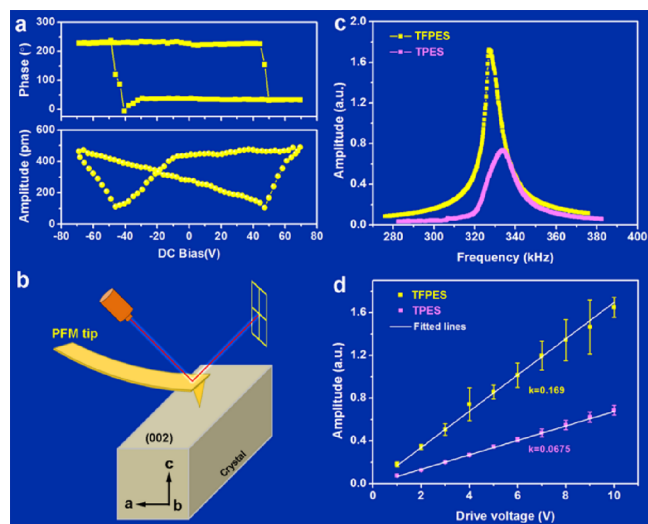


Figure 5. (a) Vertical PFM amplitude and phase signals as functions of the tip voltage for a selected point on the thin-film surface, showing local PFM hysteresis loops. (b) Schematic diagram of local piezoresponse measurements on the TFPES and TPES crystals. (c) Intrinsic amplitude signal versus driving frequency under a drive voltage of 10 V. (d) Intrinsic amplitude signal as a function of AC drive voltages.

dividing the Q factor. Figure 5c shows the SHO fitting curves of the intrinsic amplitude versus frequency for both crystals, where the stronger resonance peak is observed in the TFPES crystal under the same drive voltage of 10 V. Furthermore, such resonance measurements have been repeated under different drive voltages ranging from 1 to 10 V and over five arbitrary points across the crystals. The intrinsic amplitude was plotted against the drive voltage for both crystals, which shows good linearity. The slope of the linear curves represents the magnitude of the piezoresponse. Here, it can represent the relative magnitude of the piezoelectric constant d_{33} because the crystals are driven along the c -axis in the vertical PFM mode. By comparing the slope of the curves, the d_{33} of TFPES is 2.5 times that of TPES. This indicates that the H/F substitution can enhance the piezoelectric properties of the crystals, as previously reported in the literature.⁴² In addition, the softness of the thin film of TFPES was investigated by nanoindentation. As shown in Figure S10, the typical load–displacement curves of the TFPES thin film can be obtained, where the elastic modulus and hardness are calculated to be 411.6 and 52.7 MPa, respectively. Such a relatively low elastic modulus and hardness make the TFPES thin film a competitive candidate for flexible electronics with soft and pliable properties.

In summary, we have demonstrated the application of the H/F substitution strategy to organic single-component ferroelectrics and successfully designed an organosilicon ferroelectric crystal TFPES. Fluorination results in very small changes in the molecular arrangement and intermolecular interactions in the crystal lattice but large differences in chemical or physical properties. Compared with the parent nonferroelectric TPES and chlorinated TCPES, the synergistic effect of C–H $\cdots\pi$ interactions and F $\cdots\pi$ interactions in TFPES makes the molecules have more possibility for twist displacement, which induces a structural phase transition at a high T_c of 475 K, offering a space and opportunity for polarization switching. To our knowledge, the T_c of TFPES is the highest one among the reported organic single-component ferro-

electrics. In addition, fluorination also brought about a significant improvement in the piezoelectric performance. This finding sheds light on the exploration of high- T_c organosilicon ferroelectric crystals with great application prospects for biomedical and flexible electronic devices.

EXPERIMENTAL SECTION

Materials

All reagents and solvents in the syntheses were of reagent grade and used without further purification. The synthesis procedures of the compounds are detailedly described in the Supporting Information. The colorless crystals of TFPES were easily obtained by slow evaporation of its tetrahydrofuran solution at room temperature. The powder X-ray diffraction data show the good phase purity of these single crystals (Figure S10). Thermogravimetric analysis (TGA) shows that TPES, TFPES, TCPES, and TBPES possess good thermal stability up to 540, 550, 600, and 427 K, respectively (Figure S11).

Thin-Film Preparation

The thin films were prepared through a drop-casting method. The precursor solution of TFPES was prepared by dissolving 50 mg of the crystals in 1 mL of tetrahydrofuran. Then, 20 μ L of precursor solution was spread on a clean indium-doped tin oxide (ITO) glass substrate. The thin film was obtained after annealing at 323 K for 0.5 h.

Measurements

Methods of X-ray diffraction, DSC, SHG, Hirshfeld surface analysis, dielectric, PFM, and P – V hysteresis loop measurements are detailedly described in the Supporting Information. The X-ray crystallographic structures have been deposited at the Cambridge Crystallographic Data Centre (deposition numbers CCDC 2221431–2221433 and 2233508) and can be obtained free of charge from the CCDC via www.ccdc.cam.ac.uk/getstructures.

ASSOCIATED CONTENT

Supporting Information

The Supporting Information is available free of charge at <https://pubs.acs.org/doi/10.1021/jacsau.3c00004>.

Synthesis of samples, measurement methods, additional crystal structures, electrostatic potential maps, DSC curves, PXRD patterns, load–displacement curve, TGA curves, and crystal data (PDF)

X-ray crystallographic data for TPES at 300 K (CIF)

X-ray crystallographic data for TFPES at 300 K (CIF)

X-ray crystallographic data for TCPES at 300 K (CIF)

X-ray crystallographic data for TBPES at 300 K (CIF)

AUTHOR INFORMATION

Corresponding Authors

Ren-Gen Xiong – Ordered Matter Science Research Center, Nanchang University, Nanchang 330031, People's Republic of China; orcid.org/0000-0003-2364-0193; Email: xiongrg@seu.edu.cn

Han-Yue Zhang – State Key Laboratory of Bioelectronics, Southeast University, Nanjing 211189, People's Republic of China; orcid.org/0000-0001-6718-0665; Email: zhanghanyue@seu.edu.cn

Authors

Hang Peng – Ordered Matter Science Research Center, Nanchang University, Nanchang 330031, People's Republic of China

Hang Yu – Ordered Matter Science Research Center, Nanchang University, Nanchang 330031, People's Republic of China

Shu-Yu Tang – Ordered Matter Science Research Center, Nanchang University, Nanchang 330031, People's Republic of China

Yu-Ling Zeng – Ordered Matter Science Research Center, Nanchang University, Nanchang 330031, People's Republic of China

Peng-Fei Li – Ordered Matter Science Research Center, Nanchang University, Nanchang 330031, People's Republic of China

Yuan-Yuan Tang – Ordered Matter Science Research Center, Nanchang University, Nanchang 330031, People's Republic of China; orcid.org/0000-0002-8369-572X

Zhi-Xu Zhang – State Key Laboratory of Bioelectronics, Southeast University, Nanjing 211189, People's Republic of China; orcid.org/0000-0001-7826-8064

Complete contact information is available at: <https://pubs.acs.org/10.1021/jacsau.3c00004>

Author Contributions

#H.P. and H.Y. contributed equally. CRediT: **Hang Yu** data curation, formal analysis; **Zhi-Xu Zhang** formal analysis, writing-original draft; **Ren-Gen Xiong** conceptualization, funding acquisition, methodology, supervision, writing-review & editing; .

Author Contributions

CRediT: **Hang Peng** methodology, writing-original draft; **Hang Yu** data curation, formal analysis; **Shu-Yu Tang** data curation, resources; **Yu-Ling Zeng** data curation, formal analysis; **Peng-Fei Li** data curation, software; **Yuan-Yuan Tang** writing-review & editing; **Zhi-Xu Zhang** formal analysis, writing-original draft; **Ren-Gen Xiong** conceptualization, funding acquisition, methodology, supervision, writing-review & editing; **Han-Yue Zhang** conceptualization, data curation, formal analysis, funding acquisition, investigation, methodology, writing-review & editing.

Notes

The authors declare no competing financial interest.

ACKNOWLEDGMENTS

This work was supported by the seventh Youth Elite Scientist Sponsorship Program by the China Association for Science and Technology, the Ten Science and Technology Problem of Southeast University, and the National Natural Science Foundation of China (21991142 and 21831004).

REFERENCES

- (1) Fu, D. W.; Cai, H. L.; Liu, Y.; Ye, Q.; Zhang, W.; Zhang, Y.; Chen, X. Y.; Giovannetti, G.; Capone, M.; Li, J.; Xiong, R. G. Diisopropylammonium bromide is a high-temperature molecular ferroelectric crystal. *Science* **2013**, *339*, 425–428.
- (2) Harada, J.; Kawamura, Y.; Takahashi, Y.; Uemura, Y.; Hasegawa, T.; Taniguchi, H.; Maruyama, K. Plastic/ferroelectric crystals with easily switchable polarization: low-voltage operation, unprecedentedly high pyroelectric performance, and large piezoelectric effect in polycrystalline forms. *J. Am. Chem. Soc.* **2019**, *141*, 9349–9357.
- (3) Hu, Y.; You, L.; Xu, B.; Li, T.; Morris, S. A.; Li, Y.; Zhang, Y.; Wang, X.; Lee, P. S.; Fan, H. J.; Wang, J. Ferroelastic-switching-driven large shear strain and piezoelectricity in a hybrid ferroelectric. *Nat. Mater.* **2021**, *20*, 612–617.

- (4) Li, K.; Li, Z.-G.; Xu, J.; Qin, Y.; Li, W.; Stroppa, A.; Butler, K. T.; Howard, C. J.; Dove, M. T.; Cheetham, A. K.; Bu, X.-H. Origin of Ferroelectricity in Two Prototypical Hybrid Organic–Inorganic Perovskites. *J. Am. Chem. Soc.* **2022**, *144*, 816–823.

- (5) Liao, W.-Q.; Zhao, D.; Tang, Y.-Y.; Zhang, Y.; Li, P.-F.; Shi, P.-P.; Chen, X.-G.; You, Y.-M.; Xiong, R.-G. A molecular perovskite solid solution with piezoelectricity stronger than lead zirconate titanate. *Science* **2019**, *363*, 1206–1210.

- (6) Tang, Y. Y.; Li, P. F.; Liao, W. Q.; Shi, P. P.; You, Y. M.; Xiong, R. G. Multiaxial Molecular Ferroelectric Thin Films Bring Light to Practical Applications. *J. Am. Chem. Soc.* **2018**, *140*, 8051–8059.

- (7) Xu, H.; Guo, W.; Ma, Y.; Liu, Y.; Hu, X.; Hua, L.; Han, S.; Liu, X.; Luo, J.; Sun, Z. Record high- T_c and large practical utilization level of electric polarization in metal-free molecular antiferroelectric solid solutions. *Nat. Commun.* **2022**, *13*, 5329.

- (8) You, Y.-M.; Liao, W.-Q.; Zhao, D.; Ye, H.-Y.; Zhang, Y.; Zhou, Q.; Niu, X.; Wang, J.; Li, P.-F.; Fu, D.-W.; Wang, Z.; Gao, S.; Yang, K.; Liu, J.-M.; Li, J.; Yan, Y.; Xiong, R.-G. An organic-inorganic perovskite ferroelectric with large piezoelectric response. *Science* **2017**, *357*, 306.

- (9) Goldsmith, G. J.; White, J. G. Ferroelectric Behavior of Thiourea. *J. Chem. Phys.* **1959**, *31*, 1175–1187.

- (10) Bordeaux, D.; Bornarel, J.; Capiomont, A.; Lajzerowicz-Bonneteau, J.; Lajzerowicz, J.; Legrand, J. F. New Ferroelastic-Ferroelectric Compound: Tanane. *Phys. Rev. Lett.* **1973**, *31*, 314–317.

- (11) Kamishina, Y.; Akishige, Y.; Hashimoto, M. Ferroelectric Activity on Organic Crystal Trichloroacetamide. *J. Phys. Soc. Jpn.* **1991**, *60*, 2147–2150.

- (12) Horiuchi, S.; Tokunaga, Y.; Giovannetti, G.; Picozzi, S.; Itoh, H.; Shimano, R.; Kumai, R.; Tokura, Y. Above-room-temperature ferroelectricity in a single-component molecular crystal. *Nature* **2010**, *463*, 789.

- (13) Owczarek, M.; Hujsak, K. A.; Ferris, D. P.; Prokofjevs, A.; Majerz, I.; Szklarz, P.; Zhang, H.; Sarjeant, A. A.; Stern, C. L.; Jakubas, R.; Hong, S.; Dravid, V. P.; Stoddart, J. F. Flexible ferroelectric organic crystals. *Nat. Commun.* **2016**, *7*, 13108.

- (14) Li, P.-F.; Liao, W.-Q.; Tang, Y.-Y.; Qiao, W.; Zhao, D.; Ai, Y.; Yao, Y.-F.; Xiong, R.-G. Organic enantiomeric high- T_c ferroelectrics. *Proc. Natl. Acad. Sci. U. S. A.* **2019**, *116*, 5878–5885.

- (15) Ai, Y.; Zeng, Y.-L.; He, W.-H.; Huang, X.-Q.; Tang, Y.-Y. Six-Fold Vertices in a Single-Component Organic Ferroelectric with Most Equivalent Polarization Directions. *J. Am. Chem. Soc.* **2020**, *142*, 13989–13995.

- (16) Li, P.-F.; Ai, Y.; Zeng, Y.-L.; Liu, J.-C.; Xu, Z.-K.; Wang, Z.-X. Highest- T_c single-component homochiral organic ferroelectrics. *Chem. Sci.* **2022**, *13*, 657–664.

- (17) Song, X.-J.; Tang, S.-Y.; Chen, X.-G.; Ai, Y. Chemical design of homochiral heterocyclic organic ferroelectric crystals. *Chem. Commun.* **2022**, *58*, 10361–10364.

- (18) Lines, M. E., Glass, A. M., *Principles and applications of ferroelectrics and related materials*. Oxford university press: 2001, DOI: [10.1093/acprof:oso/9780198507789.001.0001](https://doi.org/10.1093/acprof:oso/9780198507789.001.0001).

- (19) Haertling, G. H. Ferroelectric Ceramics: History and Technology. *J. Am. Ceram. Soc.* **1999**, *82*, 797–818.

- (20) Scott, J. F. Applications of Modern Ferroelectrics. *Science* **2007**, *315*, 954.

- (21) Uchino, K., *Ferroelectric devices*. CRC press: 2018, DOI: [10.1201/b15852](https://doi.org/10.1201/b15852).

- (22) Whatmore, R. W.; You, Y.-M.; Xiong, R.-G.; Eom, C.-B. 100 years of ferroelectricity—A celebration. *APL Mater.* **2021**, *9*, No. 070401.

- (23) Li, F.; Lin, D.; Chen, Z.; Cheng, Z.; Wang, J.; Li, C.; Xu, Z.; Huang, Q.; Liao, X.; Chen, L.-Q.; ShROUT, T. R.; Zhang, S. Ultrahigh piezoelectricity in ferroelectric ceramics by design. *Nat. Mater.* **2018**, *17*, 349–354.

- (24) Batlogg, B.; Cava, R. J.; Jayaraman, A.; van Dover, R. B.; Kourouklis, G. A.; Sunshine, S.; Murphy, D. W.; Rupp, L. W.; Chen, H. S.; White, A.; Short, K. T.; Mujcsce, A. M.; Rietman, E. A. Isotope

Effect in the High- T_c Superconductors $Ba_2YCu_3O_7$ and $Ba_2EuCu_3O_7$. *Phys. Rev. Lett.* **1987**, *58*, 2333–2336.

(25) Zhang, K.; Liu, J.; Lin, H.; Wang, N.; Zhao, K.; Zhang, A.; Jin, F.; Zhong, Y.; Hu, X.; Duan, W.; Zhang, Q.; Fu, L.; Xue, Q.-K.; Chen, X.; Ji, S.-H. Discovery of robust in-plane ferroelectricity in atomic-thick SnTe. *Science* **2016**, *353*, 274–278.

(26) Zhang, L.; Chen, J.; Fan, L.; Dieguez, O.; Cao, J.; Pan, Z.; Wang, Y.; Wang, J.; Kim, M.; Deng, S.; Wang, J.; Wang, H.; Deng, J.; Yu, R.; Scott, J. F.; Xing, X. Giant polarization in super-tetragonal thin films through interphase strain. *Science* **2018**, *361*, 494–497.

(27) Blinc, R. On the isotopic effects in the ferroelectric behaviour of crystals with short hydrogen bonds. *J. Phys. Chem. Solids* **1960**, *13*, 204–211.

(28) Katrusiak, A. Geometric effects of H-atom disordering in hydrogen-bonded ferroelectrics. *Phys. Rev. B* **1993**, *48*, 2992–3002.

(29) Koval, S.; Kohanoff, J.; Migoni, R. L.; Tosatti, E. Ferroelectricity and Isotope Effects in Hydrogen-Bonded KDP Crystals. *Phys. Rev. Lett.* **2002**, *89*, No. 187602.

(30) Negran, T. J.; Glass, A. M.; Brickenkamp, C. S.; Rosenstein, R. D.; Osterheld, R. K.; Susott, R. Ferroelectricity in lead monohydrogen phosphate, $PbHPO_4$, and the deuterated form, $PbDPO_4$. *Ferroelectrics* **1973**, *6*, 179–182.

(31) Shi, C.; Zhang, X.; Yu, C.-H.; Yao, Y.-F.; Zhang, W. Geometric isotope effect of deuteration in a hydrogen-bonded host–guest crystal. *Nat. Commun.* **2018**, *9*, 481.

(32) Ai, Y.; Lv, H.-P.; Wang, Z.-X.; Liao, W.-Q.; Xiong, R.-G. H/F substitution for advanced molecular ferroelectrics. *Trends Chem.* **2021**, *3*, 1088–1099.

(33) Liu, H.-Y.; Zhang, H.-Y.; Chen, X.-G.; Xiong, R.-G. Molecular Design Principles for Ferroelectrics: Ferroelectrochemistry. *J. Am. Chem. Soc.* **2020**, *142*, 15205–15218.

(34) Mu, X.; Zhang, H.-Y.; Xu, L.; Xu, Y.-Y.; Peng, H.; Tang, Y.-Y.; Xiong, R.-G. Ferroelectrochemistry. *APL Mater.* **2021**, *9*, No. 051112.

(35) Ai, Y.; Chen, X.-G.; Shi, P.-P.; Tang, Y.-Y.; Li, P.-F.; Liao, W.-Q.; Xiong, R.-G. Fluorine Substitution Induced High T_c of Enantiomeric Perovskite Ferroelectrics: (R)- and (S)-3-(Fluoropyrrolidinium) $MnCl_3$. *J. Am. Chem. Soc.* **2019**, *141*, 4474–4479.

(36) Tang, Y.-Y.; Xie, Y.; Ai, Y.; Liao, W.-Q.; Li, P.-F.; Nakamura, T.; Xiong, R.-G. Organic Ferroelectric Vortex–Antivortex Domain Structure. *J. Am. Chem. Soc.* **2020**, *142*, 21932–21937.

(37) Zhang, H.-Y.; Song, X.-J.; Chen, X.-G.; Zhang, Z.-X.; You, Y.-M.; Tang, Y.-Y.; Xiong, R.-G. Observation of Vortex Domains in a Two-Dimensional Lead Iodide Perovskite Ferroelectric. *J. Am. Chem. Soc.* **2020**, *142*, 4925–4931.

(38) Ai, Y.; Wu, D.-J.; Yang, M.-J.; Wang, P.; He, W.-H.; Liao, W.-Q. Highest- T_c organic enantiomeric ferroelectrics obtained by F/H substitution. *Chem. Commun.* **2020**, *56*, 7033–7036.

(39) Deng, B.-B.; Xu, C.-C.; Cheng, T.-T.; Yang, Y.-T.; Hu, Y.-T.; Wang, P.; He, W.-H.; Yang, M.-J.; Liao, W.-Q. Homochiral Nickel Nitrite ABX_3 ($X = NO_2^-$) Perovskite Ferroelectrics. *J. Am. Chem. Soc.* **2020**, *142*, 6946–6950.

(40) Tang, Y.-Y.; Ai, Y.; Liao, W.-Q.; Li, P.-F.; Wang, Z.-X.; Xiong, R.-G. H/F-Substitution-Induced Homochirality for Designing High- T_c Molecular Perovskite Ferroelectrics. *Adv. Mater.* **2019**, *31*, No. 1902163.

(41) Xie, Y.; Ai, Y.; Zeng, Y.-L.; He, W.-H.; Huang, X.-Q.; Fu, D.-W.; Gao, J.-X.; Chen, X.-G.; Tang, Y.-Y. The Soft Molecular Polycrystalline Ferroelectric Realized by the Fluorination Effect. *J. Am. Chem. Soc.* **2020**, *142*, 12486–12492.

(42) Zhang, H.-Y.; Zhang, Z.-X.; Song, X.-J.; Chen, X.-G.; Xiong, R.-G. Two-Dimensional Hybrid Perovskite Ferroelectric Induced by Perfluorinated Substitution. *J. Am. Chem. Soc.* **2020**, *142*, 20208–20215.

(43) Tang, Y.-Y.; Xie, Y.; Zeng, Y.-L.; Liu, J.-C.; He, W.-H.; Huang, X.-Q.; Xiong, R.-G. Record Enhancement of Phase Transition Temperature Realized by H/F Substitution. *Adv. Mater.* **2020**, *32*, No. 2003530.

(44) Zhang, Z.-X.; Song, X.-J.; Li, Y.-R.; Chen, X.-G.; Zhang, Y.; Lv, H.-P.; Tang, Y.-Y.; Xiong, R.-G.; Zhang, H.-Y. The First Chiro-Inositol Organosilicon Ferroelectric Crystal. *Angew. Chem., Int. Ed.* **2022**, *61*, No. e202210809.

(45) Colas, A.; Curtis, J. Silicone biomaterials: history and chemistry. *Biomater. Sci.* **2004**, *2*, 80–85.

(46) Komiyama, T.; Minami, Y.; Hiyama, T. Recent Advances in Transition-Metal-Catalyzed Synthetic Transformations of Organosilicon Reagents. *ACS Catal.* **2016**, *7*, 631–651.

(47) Rucker, C.; Kummerer, K. Environmental chemistry of organosiloxanes. *Chem. Rev.* **2015**, *115*, 466–524.

(48) Xu, L.-W.; Li, L.; Lai, G.-Q.; Jiang, J.-X. The recent synthesis and application of silicon-stereogenic silanes: A renewed and significant challenge in asymmetric synthesis. *Chem. Soc. Rev.* **2011**, *40*, 1777–1790.

(49) Franz, A. K.; Wilson, S. O. Organosilicon Molecules with Medicinal Applications. *J. Med. Chem.* **2012**, *56*, 388–405.

(50) Zeng, Y.-L.; Ai, Y.; Tang, S.-Y.; Song, X.-J.; Chen, X.-G.; Tang, Y.-Y.; Zhang, Z.-X.; You, Y.-M.; Xiong, R.-G.; Zhang, H.-Y. Axial-Chiral BINOL Multiferroic Crystals with Coexistence of Ferroelectricity and Ferroelasticity. *J. Am. Chem. Soc.* **2022**, *144*, 19559–19566.

(51) Pauling, L., *The Nature of the Chemical Bond*; Cornell University Press, Ithaca, New York, 1960.

(52) Aizu, K. Possible species of ferromagnetic, ferroelectric, and ferroelastic crystals. *Phys. Rev. B* **1970**, *2*, 754.

(53) Jiang, P.; Huang, B.; Wei, L.; Yan, F.; Huang, X.; Li, Y.; Xie, S.; Pan, K.; Liu, Y.; Li, J. Resolving fine electromechanical structure of collagen fibrils via sequential excitation piezoresponse force microscopy. *Nanotechnology* **2019**, *30*, No. 205703.